

A wavelet based method for image reconstruction from gradient data with applications

Ioana S. Sevcenco · Peter J. Hampton ·
Panajotis Agathoklis

Received: 5 February 2013 / Revised: 11 September 2013 / Accepted: 15 October 2013 /
Published online: 7 November 2013
© Springer Science+Business Media New York 2013

Abstract In this paper, an algorithm for image reconstruction from gradient data based on the Haar wavelet decomposition is proposed. The proposed algorithm has two main stages. First, the Haar decomposition of the image to be reconstructed is obtained from the given gradient data set. Then, the Haar wavelet synthesis is employed to produce the image. The proposed algorithm is based on the relationship between the Haar analysis and synthesis filters and the model for the discretized gradient. The approach presented here is based on the one by Hampton et al. (IEEE J Sel Top Signal Process 2(5):781–792, 2008) for wavefront reconstruction in adaptive optics. The main strength of the proposed algorithm lies in its multi-resolution nature, which allows efficient processing in the wavelet domain with complexity $\mathcal{O}(N)$. In addition, obtaining the wavelet decomposition of the image to be reconstructed provides the possibility for further enhancements of the image, such as denoising or smoothing via iterative Poisson solvers at each resolution during Haar synthesis. To evaluate the performance of the proposed algorithm, it is applied to reconstruct ten standard test images. Experiments demonstrate that the algorithm yields results comparable in terms of solution accuracy to those produced by well-known benchmark algorithms. Further, experiments show that the proposed algorithm is suitable to be employed as a final step to reconstruct an image from a gradient data set, in applications such as image stitching or image morphing.

Keywords Image reconstruction · Gradient · Haar decomposition · Poisson solver

I. S. Sevcenco (✉) · P. Agathoklis
Department of Electrical and Computer Engineering, University of Victoria,
Victoria, BC V8P 5C2, Canada
e-mail: ioana.sevcenco@ece.uvic.ca

P. Agathoklis
e-mail: pan@ece.uvic.ca

P. J. Hampton
307-720 Eighth Avenue, New Westminster V3M 2R3, Canada
e-mail: peterjhampton@ieee.org

1 Introduction

In the last decades, the development of effective methods to recover surfaces from gradient data sets has been subject of intense research interest due to many applications such as shape from shading (Frankot and Chellappa 1988), generating panoramic images (Levin et al. 2004), editing digital images (Perez et al. 2003; Agrawal et al. 2005; Finlayson et al. 2002), high dynamic range compression (Fattal et al. 2002), face recognition (Smith and Hancock 2006), medical imaging (Craine et al. 1998), estimating wavefronts in adaptive optics (Hampton et al. 2008) and the development of gradient cameras (Tumblin et al. 2005). In this paper, the term *gradient* denotes the rate of change in intensity between neighbouring pixels in an image. An important motivation in many of these applications is the fact that the human visual system is more sensitive to local contrast than to absolute values of light intensity (Rash et al. 2009). Local contrast, viewed as local differences between light intensity values of adjacent points in a scene, corresponds to differentiation. Naturally then, effective solutions to important real life applications from different fields have been sought and found in the gradient domain.

A typical approach in these applications is to generate a gradient of the desired image or surface and an important step in these applications is to recover the image or surface from the previously created gradient data set. This should be achieved via two dimensional (2D) integration and the main challenge is the fact that the given gradient data set is often times not integrable. That is, the given gradient violates the zero curl condition, according to which the integral along any closed path is zero, and the result of the integration is path independent. Therefore, typical approaches to recover surfaces or images from their gradient are: Poisson solvers (Watkins 2002), identifying and minimizing the nonzero part of the curl (Reddy et al. 2009), or projecting the given gradient onto a space where the zero curl condition is satisfied (Frankot and Chellappa 1988; Simchony et al. 1990).

Shape from shading (Frankot and Chellappa 1988; Simchony et al. 1990; Agrawal and Raskar 2006) and photometric stereo (Hertzmann and Seitz 2005) are well known problems in computer vision, with applications ranging from industrial measurement and remote sensing to medical imaging and face recognition. Shape from shading algorithms aim to recover the shape of a three dimensional object from a single 2D representation of that object, such as a digital image. Photometric stereo denotes a special case of shape from shading, where more images of the same object are used to determine the three dimensional shape of the object. A well known approach in shape from shading is the Frankot-Chellappa algorithm (1988). In this method, the given gradient data is integrated in the Fourier domain and then an estimate of the surface is obtained by inverting the transform. Similarly, Simchony et al. (1990) obtain a surface estimate by operating on the discrete cosine transform (DCT) coefficients, while the approach of Kovési (2005) employs shapelets basis functions. Agrawal and Raskar (2006) propose a general framework for surface reconstruction from gradients and perform a comparative study in the presence of noise and outliers. More recently, Harker and O'Leary (2008) put forth an algebraic approach to integrate a gradient field in the discrete domain. They express the global least squares objective function in terms of matrix algebra and show that the minimizer (unique, up to a constant of integration) can be obtained as the solution to a Lyapunov equation. Their work is further developed in Harker and O'Leary (2013a, b), handling regularization problems associated with surface reconstruction from gradient.

Adaptive optics is another area where gradient data obtained from wavefront sensors is used to reconstruct an estimate of the wavefront. The model for the gradient used in adaptive optics is related to the Shack-Hartmann wavefront sensor and is different

than the one used in computer vision applications. The adaptive optics gradient model is called the Fried model (Fried 1977) and essentially approximates the gradient at the center of four pixels, whereas the gradient used in vision applications, called the Hudgin model (Hudgin 1977) in adaptive optics, approximates the gradient between two vertical pixels and two horizontal pixels. Several fast methods for wavefront reconstruction have been developed, such as multigrid conjugate gradient methods (Gilles et al. 2002; Vogel and Yang 2006) or Fourier transform techniques (Poyneer and Véran 2005), similar to those used in computer vision. Recently, a 2D integration method (Hampton et al. 2008) has been presented and applied to image reconstruction for adaptive optics. In this method, a Haar decomposition of the associated image is directly obtained from the image gradient measurements and then using the well known Haar synthesis algorithm the image is reconstructed. This method has been shown (Hampton et al. 2008) to have a computational complexity that increases linearly with the number of data points and allows performing denoising by using the High-High region of the Haar decomposition. Finally the multiresolution nature of this algorithm allows the iterative solution of the Poisson equation at various resolutions (Hampton and Agathoklis 2010; Sevcenco et al. 2011).

In this paper an image reconstruction technique from gradient data, which can be used in applications such as future digital gradient cameras as well as in other image processing and computer vision applications, is proposed. The approach proposed here is based on extending the image reconstruction method proposed by Hampton et al. (2008) to the case of using gradient data modeled by the Hudgin geometry. Further, an iterative Poisson solver at each resolution of the Haar synthesis process is included, as previously suggested (Hampton and Agathoklis 2010; Sevcenco et al. 2011), to deal with the cases where the gradient data may not satisfy the curl equal zero condition. This is common in applications where the gradient data used for reconstruction has undergone editing transformations that lead to the curl equal zero condition not being satisfied. The addition of the iterative Poisson solver leads to a more accurate reconstruction of images containing significant amounts of high frequency detail. In the proposed extended technique, similarly as in the original method of Hampton et al. (2008), the Haar decomposition is obtained first. Then, Haar synthesis is applied to obtain image estimates at increasing resolutions. At each resolution, a Poisson solver is used to iteratively improve the estimate of the image at this resolution.

The organization of this paper is as follows. In Sect. 2, the two main models of discrete differentiation are presented and some of the necessary definitions of the Haar wavelet transform are summarized. In Sect. 3, the problem of image reconstruction from gradient data and its relation to the Poisson equation is briefly reviewed. Then, a reconstruction algorithm based on wavelets is introduced which is an extension of the one proposed by Hampton et al. (2008). In Sect. 4, the proposed algorithm is used to reconstruct images from different gradient data sets and its performance is compared with other algorithms. In Sect. 5, it is illustrated how the proposed algorithm can be used in two image processing applications.

2 Preliminaries

2.1 The Haar wavelet decomposition of an image

The Haar wavelet decomposition of an image will be used in this paper. The Haar analysis filters (Vetterli and Kovačević 1995) are given by:

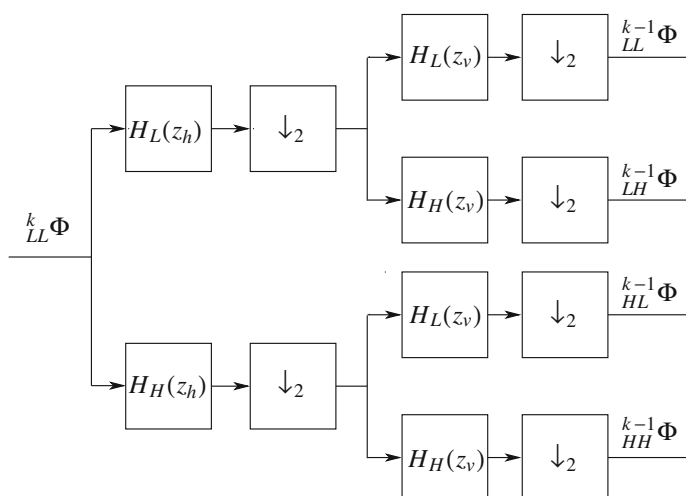


Fig. 1 Obtaining one level from another in a Haar wavelet decomposition. z_v and z_h indicate vertical and horizontal filtering, respectively

$$H_L(z) = \frac{1}{\sqrt{2}} (1 + z^{-1}) \quad (1)$$

$$H_H(z) = \frac{1}{\sqrt{2}} (1 - z^{-1}) \quad (2)$$

For a grayscale image Φ of size $2^M \times 2^M$, successive filtering with the Haar wavelet analysis filters and downsampling as shown in the diagram in Fig. 1 yield a decomposition as the one in Fig. 2. In Fig. 1, z_v and z_h indicate vertical and horizontal filtering, respectively. It is well known that this process is reversible and the original image can be fully recovered by upsampling and filtering with the Haar wavelet synthesis filters.

$$G_L(z) = H_L(z^{-1}) = \frac{1}{\sqrt{2}} (1 + z) \quad (3)$$

$$G_H(z) = H_H(z^{-1}) = \frac{1}{\sqrt{2}} (1 - z) \quad (4)$$

The standard Haar wavelet decomposition of an image Φ of size $2^M \times 2^M$ is shown in Fig. 2. At level k , the decomposition has four main subbands: Φ_{HH}^{k-1} , Φ_{HL}^{k-1} , Φ_{LH}^{k-1} and Φ_{LL}^{k-1} . The size of each subband is $2^{k-1} \times 2^{k-1}$. By convention, level M corresponds to the full resolution image, i.e. $\Phi_{LL}^M = \Phi$. The order of subscript indices H and L holds information about the order in which the Haar wavelet analysis filters must be applied to the LL subband at level $k + 1$ in order to obtain the four subbands at the following level k .

2.2 The discretization of image gradients

Two approximation models are typically employed to compute the gradient of a digital image. These models have been adopted in image processing (Fattal et al. 2002; Levin et al. 2004; Tumblin et al. 2005), computer vision (Agrawal and Raskar 2006; Reddy et al. 2009; Kovese 2005) as well as adaptive optics (Hampton et al. 2008) algorithms, mainly due to their simplicity and ease of computation. The two models have in common a finite differencing

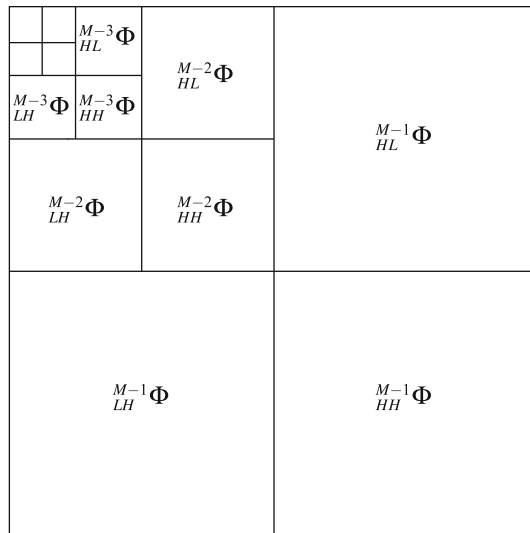


Fig. 2 Standard Haar wavelet decomposition of a 2D image

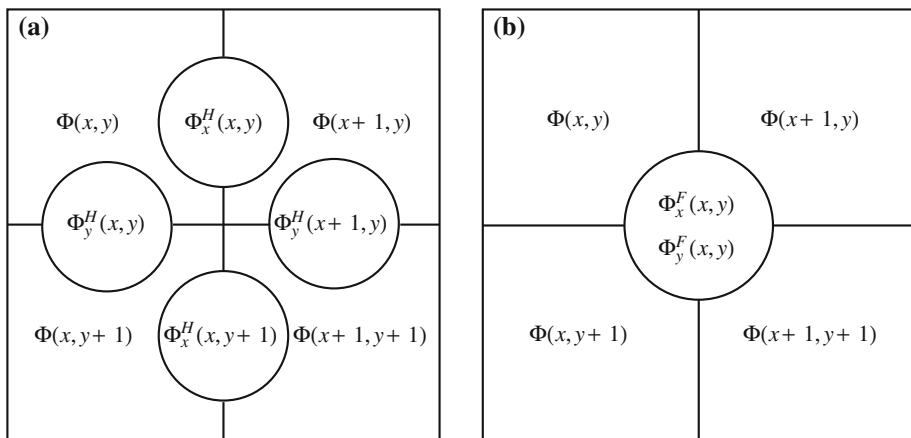


Fig. 3 Commonly employed geometries for computing image derivatives. **a** Hudgin geometry. **b** Fried geometry

step between neighbouring pixel intensity values, but approximate the gradient at different locations as discussed shortly. The first approximation model is commonly used in image processing (Levin et al. 2004) and computer vision (Agrawal and Raskar 2006). In adaptive optics literature this approximation model is referred to as the Hudgin gradient geometry (Hudgin 1977). In this model, the continuous derivatives are approximated between two vertical and two horizontal pixels, as shown in Fig. 3a. The second approximation model for computing the gradient of a digital image is the Fried model (Fried 1977). This approximation model is widely used in adaptive optics because it matches the geometry of the Shack-Hartmann wavefront sensors. This model approximates the continuous derivative value at the center of a four point pixel grid, as illustrated in Fig. 3b.

The full resolution gradient components of an image Φ of size $2^M \times 2^M$ are denoted by Φ_x^H , Φ_y^H , ${}^M\Phi_x$, and ${}^M\Phi_y$, in Hudgin and Fried alignment, respectively. Mathematically, the Hudgin gradient of an image Φ of size $M \times N$ is defined by its two components of size $(M-1) \times N$ and $M \times (N-1)$, with elements given by:

$$\Phi_x^H(x, y) = \Phi(x+1, y) - \Phi(x, y) \quad (5)$$

$$\Phi_y^H(x, y) = \Phi(x, y+1) - \Phi(x, y) \quad (6)$$

The Fried gradient is described by its two components of size $(M-1) \times (N-1)$, whose elements are given by:

$$\begin{aligned} \Phi_x^F(x, y) &= 0.5 [\Phi_x^H(x, y) + \Phi_x^H(x, y+1)] \\ &= 0.5 [\Phi(x+1, y) - \Phi(x, y) + \Phi(x+1, y+1) - \Phi(x, y+1)] \end{aligned} \quad (7)$$

and

$$\begin{aligned} \Phi_y^F(x, y) &= 0.5 [\Phi_y^H(x, y) + \Phi_y^H(x+1, y)] \\ &= 0.5 [\Phi(x, y+1) - \Phi(x, y) + \Phi(x+1, y+1) - \Phi(x+1, y)] \end{aligned} \quad (8)$$

The connection between the two discretization models is straightforward and can be observed from Eqs. (5)–(8). That is, the value of a Fried directional derivative is the average of two neighbouring Hudgin directional derivatives.

The connection between the two previously described gradient approximation schemes and the Haar filters is interesting. The Hudgin gradient can be obtained from the image by filtering it with a scaled version of the Haar analysis highpass filter. Following this idea, it can be seen that the Fried gradient can be obtained by filtering each Hudgin image gradient component with a scaled version of the Haar analysis lowpass filter. Thus, the relationship between the Hudgin and Fried gradients to the Haar wavelet filters is characterized by:

$$\Phi_x^F = \frac{1}{\sqrt{2}} \Phi_x^H H_L(z_v) \quad (9)$$

$$\Phi_y^F = \frac{1}{\sqrt{2}} \Phi_y^H H_L(z_h) \quad (10)$$

where the notation $\Phi H(z)$ means filtering the data set Φ with a one-dimensional filter with transfer function $H(z)$.

A graphical representation of how the gradients can be obtained from an image by directional filtering with scaled Haar wavelet filters can be seen in Fig. 4. This connection between the two gradient approximation schemes and the Haar filters is what underlies the reconstruction algorithm presented in the following section.

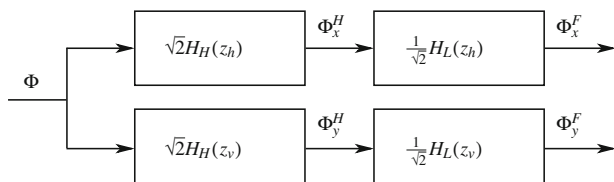


Fig. 4 Hudgin and Fried derivatives computed via scaled Haar wavelet filtering. z_h and z_v indicate horizontal and vertical filtering, respectively

3 Image reconstruction from gradient data

3.1 Problem formulation

As discussed earlier in Sect. 1, image reconstruction is a necessary step at the end of gradient based image processing algorithms. In the continuous case, the problem of image reconstruction from a given gradient data set can be formulated as follows: Given gradient data

$\tilde{\Phi} = \begin{bmatrix} \tilde{\Phi}_x \\ \tilde{\Phi}_y \end{bmatrix}$, find Φ such that

$$\nabla \Phi = \tilde{\Phi} \quad (11)$$

where the operator $\nabla = \begin{bmatrix} \frac{\partial}{\partial x} \\ \frac{\partial}{\partial y} \end{bmatrix}$ denotes the continuous gradient operator.

Problem (11) will have a meaningful solution if the given gradient is a *conservative vector field*. In the case of 2D functions such as images, the conservative field condition is equivalent to the zero curl condition and implies the equality of the second order mixed partial derivatives. Namely, Φ must satisfy the following condition:

$$\frac{\partial^2 \Phi}{\partial x \partial y} = \frac{\partial^2 \Phi}{\partial y \partial x} \quad (12)$$

Consequently, in order for Eq. (11) to have a solution, the given vector field $\tilde{\Phi}$ must satisfy:

$$\frac{\partial \tilde{\Phi}_x}{\partial y} = \frac{\partial \tilde{\Phi}_y}{\partial x} \quad (13)$$

In practice, the given gradient data set $\tilde{\Phi}$ is either directly acquired from sensors, and therefore contains measurement noise, or it is obtained from processing an integrable gradient. As a result, condition (13) may not hold in practical problems. A common approach (Simchony et al. 1990; Fattal et al. 2002; Agrawal and Raskar 2006) is then to find an estimate of the image Φ by reformulating Problem (11) as a minimization problem:

$$\min_{\Phi} \int \int \left[\left(\frac{\partial \Phi}{\partial x} - \tilde{\Phi}_x \right)^2 + \left(\frac{\partial \Phi}{\partial y} - \tilde{\Phi}_y \right)^2 \right] dx dy \quad (14)$$

A function Φ that minimizes (14) must satisfy the Euler–Lagrange equation (Fattal et al. 2002):

$$2 \left(\frac{\partial^2 \Phi}{\partial x^2} - \frac{\partial \tilde{\Phi}_x}{\partial x} \right) + 2 \left(\frac{\partial^2 \Phi}{\partial y^2} - \frac{\partial \tilde{\Phi}_y}{\partial y} \right) = 0. \quad (15)$$

Dividing both sides of Eq. (15) by 2, yields:

$$\frac{\partial^2 \Phi}{\partial x^2} - \frac{\partial \tilde{\Phi}_x}{\partial x} = \frac{\partial \tilde{\Phi}_y}{\partial y} - \frac{\partial^2 \Phi}{\partial y^2}. \quad (16)$$

As a result,

$$\frac{\partial^2 \Phi}{\partial x^2} + \frac{\partial^2 \Phi}{\partial y^2} = \frac{\partial \tilde{\Phi}_x}{\partial x} + \frac{\partial \tilde{\Phi}_y}{\partial y}. \quad (17)$$

A more compact form to write Eq. (17) is:

$$\nabla^2 \Phi = \nabla^T \cdot \tilde{\Phi} \quad (18)$$

where $\nabla^2 \Phi = \frac{\partial^2 \Phi}{\partial x^2} + \frac{\partial^2 \Phi}{\partial y^2}$ denotes the Laplacian of Φ , and the symbol \cdot is used to denote the standard inner product.

Equation (18) is known as the Poisson equation and there are various approaches to solve it, given proper boundary conditions. The approach presented in this paper is an extension of the method developed by Hampton et al. (2008), and is based on the Haar wavelet decomposition of the image to be reconstructed.

3.2 Image reconstruction from Hudgin aligned gradient

The algorithm proposed here has two main stages. In the first stage, the Haar wavelet decomposition of the image to be reconstructed is obtained directly from the given Hudgin gradient data. In the second stage, the image is obtained from the Haar wavelet decomposition via Haar wavelet synthesis. To attenuate the effects that a corrupted gradient has on the reconstruction, an iterative Poisson solver can be included during the second stage of the proposed algorithm (Hampton and Agathoklis 2010; Sevcenco et al. 2011).

Algorithm description

Analysis step: Given the Hudgin gradient components, Φ_x^H and Φ_y^H , obtain the Haar wavelet decomposition of the image.

For the upper right and lower left quadrants (HL and LH subbands of the decomposition in Fig. 2):

$${}_{HL}^{M-1} \Phi = \downarrow_2 \left\{ \frac{\Phi_x^H H_L(z_v)}{\sqrt{2}} \right\} = \downarrow_2 \left\{ {}^M \Phi_x \right\} \quad (19)$$

$${}_{LH}^{M-1} \Phi = \downarrow_2 \left\{ \frac{\Phi_y^H H_L(z_h)}{\sqrt{2}} \right\} = \downarrow_2 \left\{ {}^M \Phi_y \right\} \quad (20)$$

For the lower right quadrant (HH):

$${}_{HH}^{M-1} \Phi = \downarrow_2 \left\{ \frac{\sqrt{2}}{4} \left[\Phi_x^H H_H(z_v) + \Phi_y^H H_H(z_h) \right] \right\} \quad (21)$$

For the upper left quadrant (LL):

For $k = M$ to 2

$${}^{k-1} \Phi_x = \sqrt{2} \downarrow_2 \{ {}^k \Phi_x H_L^2(z_h) H_L(z_v^2) \} \quad (22)$$

$${}^{k-1} \Phi_y = \sqrt{2} \downarrow_2 \{ {}^k \Phi_y H_L(z_h^2) H_L^2(z_v) \} \quad (23)$$

$${}_{HL}^{k-2} \Phi = \downarrow_2 \{ {}^{k-1} \Phi_x \} \quad (24)$$

$${}_{LH}^{k-2} \Phi = \downarrow_2 \{ {}^{k-1} \Phi_y \} \quad (25)$$

$$\begin{aligned} {}_{HH}^{k-2} \Phi &= \sqrt{2} \downarrow_4 \{ {}^k \Phi_x H_L^2(z_h) H_H(z_v^2) \} \\ &= \sqrt{2} \downarrow_4 \{ {}^k \Phi_y H_H(z_h^2) H_L^2(z_v) \} \end{aligned} \quad (26)$$

Here, the downsampling and upsampling operators are represented by the symbols \downarrow and \uparrow , respectively. The downsampling and upsampling factors are indicated by subscripts on the right hand-side of the arrows. The proof of the algorithm can be found in “Appendix 1”.

Synthesis step: Given the decomposition obtained in the Analysis step (see Fig. 2), reconstruct the image by Haar wavelet synthesis. Depending on the corruption degree of the given gradient, the following two approaches can be employed to obtain the image.

Option 1. Reconstruction without Poisson smoothing

Given four subband channels at level k , subband LL of level $k + 1$ is obtained as follows: For $k = 0$ to $M - 1$

$$\begin{aligned} {}^{k+1}_{LL}\Phi &= G_L(z_h) \left[G_L(z_v) \uparrow_2 \left\{ {}^k_{LL}\Phi \right\} + G_H(z_v) \uparrow_2 \left\{ {}^k_{LH}\Phi \right\} \right] \\ &\quad + G_H(z_h) \left[G_L(z_v) \uparrow_2 \left\{ {}^k_{HL}\Phi \right\} + G_H(z_v) \uparrow_2 \left\{ {}^k_{HH}\Phi \right\} \right] \end{aligned} \quad (27)$$

Option 2. Reconstruction with Poisson smoothing

To overcome possible artifacts due to corrupted gradient data, the approach of Hampton and Agathoklis (2010) and Sevcenco et al. (2011) is adopted here and involves employing an iterative Poisson solver at each resolution level during the synthesis step. Specifically, the image estimate obtained after one level of Haar wavelet synthesis is smoothened using a Poisson solver and used to reconstruct the next level. The Poisson equation is:

$$\nabla^2 \Phi_{est} = \nabla^T \cdot \tilde{\Phi} \quad (28)$$

where Φ_{est} is the image to be reconstructed from a given gradient data set $\tilde{\Phi}$. If the Laplacian and gradient are discretized using the Fried model, Eq. (28) becomes:

$$\begin{bmatrix} 1 & 0 & 1 \\ 0 & -4 & 0 \\ 1 & 0 & 1 \end{bmatrix} \otimes \Phi_{est} = \begin{bmatrix} 1 & -1 \\ 1 & -1 \end{bmatrix} \otimes \tilde{\Phi}_x + \begin{bmatrix} 1 & 1 \\ -1 & -1 \end{bmatrix} \otimes \tilde{\Phi}_y \quad (29)$$

As has been noted in Hampton and Agathoklis (2010), Eq. (29) can be solved iteratively, using the Jacobi method. The recursion formula is:

$$\begin{aligned} \Phi_{est}[i + 1] &= \Phi_{est}[i] - \frac{1}{4} \left(\begin{bmatrix} -1 & 0 & -1 \\ 0 & 4 & 0 \\ -1 & 0 & -1 \end{bmatrix} \otimes \Phi_{est}[i] \right. \\ &\quad \left. + \begin{bmatrix} 1 & -1 \\ 1 & -1 \end{bmatrix} \otimes \tilde{\Phi}_x + \begin{bmatrix} 1 & 1 \\ -1 & -1 \end{bmatrix} \otimes \tilde{\Phi}_y \right) \end{aligned} \quad (30)$$

where i is the integer iteration index. In Eqs. (29) and (30), the symbol \otimes denotes 2D convolution. At each resolution level, the LL subband obtained from Eq. (27) is used as an initial point for the iterative process described by Eq. (30). The fact that a good initial point is provided at each resolution level ensures a fast convergence of the Poisson solver. Performing a very small number of iterations of Eq. (30) at each resolution level produces acceptable estimates of the image to be reconstructed as will be illustrated shortly, in Sect. 4 of this paper.

If this type of reconstruction is chosen, immediately after obtaining the LL subband of level $k + 1$ using Eq. (27), the LL subband is replaced by:

$$\begin{aligned} {}^{k+1}_{LL}\Phi &:= \frac{1}{2} \left\{ {}^{k+1}_{LL}\Phi z_h z_v H_L(z_h^2) H_L(z_v^2) \right. \\ &\quad \left. - {}^{k+1}\Phi_x H_H(z_h) H_L(z_v) - {}^{k+1}\Phi_y H_L(z_h) H_H(z_v) \right\} \end{aligned} \quad (31)$$

where the notation $a := b$ means that quantity a is replaced by quantity b . This substitution corresponds to performing one iteration of the recursive formula (30). The number of

iterations depends on the amount of noise, but few iterations are usually sufficient to obtain satisfactory results.

3.3 Remarks

A first remark concerns the top left entry of the LL quadrant of the decomposition obtained after the analysis step (i.e., $\overset{0}{LL}\Phi$ in Fig. 2). To complete the analysis step of the algorithm, this entry has to be defined. From wavelet theory, it is known that this entry of the Haar wavelet decomposition is proportional to the mean value of the image. So, when the input gradient is not corrupted, the reconstruction algorithm is exact if the mean value of the image to be reconstructed is known. If this value is not known, it can be estimated given the dynamic range and the size of the image to be reconstructed.

A second remark concerns the applicability of the proposed algorithm to reconstruct images of rectangular arbitrary size. In the above description of the algorithm, the image to be reconstructed is assumed to be square, of size $2^M \times 2^M$. In practice, however, the image to be reconstructed is typically rectangular, with dimensions that are not necessarily powers of 2. To address this more general case, a modification must be made to the proposed algorithm. This modification is similar in spirit to the one mentioned by Hampton et al. (2009), and involves reflecting (mirroring) the given gradient to create a data set with dimensions consistent with the ones of a gradient of a $2^M \times 2^M$ image. Care must be exercised when reflecting the given gradient, due to the particularities of the Hudgin geometry. After the reflected gradient data set is produced, the Haar wavelet decomposition of this extended structure is obtained using Eqs. (19)–(22). Then, an initial reconstruction is obtained via synthesis. Finally, the image of interest is cropped from this reconstruction. In this case, the mean value of the image, if known, is corrected at the end by a uniform shift of all pixel values.

The proposed algorithm can be applied to reconstruct color images, given their gradients. Specifically, a typical multichannel representation of a color image employs a color model such as RGB or YC_bC_r . A possible approach to obtain a color image from its Hudgin gradient is by reconstructing each individual channel of the image, using one of the two options described. The three channels are then combined into the multichannel image. Such an approach was used in the mountain example shown in Sect. 5.

4 Performance evaluation of the proposed reconstruction technique

In this section, the performance of the proposed reconstruction algorithm is evaluated and the results are compared with two benchmark existing techniques of Frankot and Chellappa (1988) and Simchony et al. (1990), as well as with two newer techniques introduced by Kovesi (2005) and Harker and O’Leary (2008). The performance is evaluated in terms of reconstruction accuracy and computational requirements. Three cases are considered: first the case of image reconstruction from noise free input gradient data, second the case of reconstructing the image from a gradient corrupted by white Gaussian noise and third the case of gradient data corrupted with outliers (impulsive noise).

4.1 Clean gradient data

The performance of the proposed method has been evaluated using gradient data from 10 images with resolutions between 64×64 and $1,024 \times 1,024$. A subset of the test images

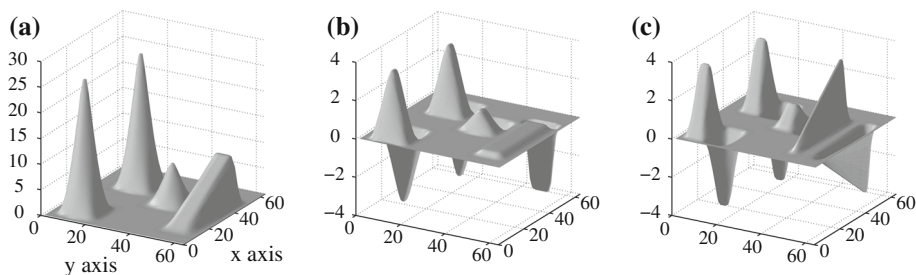


Fig. 5 Test image ramp peaks: computer generated surface and its gradient components. Image size: 64×64 . **a** Test image. **b** x gradient component. **c** y gradient component

is shown in Fig. 5a and in Fig. 6. The image ramp peaks was chosen as benchmark by Agrawal and Raskar (2006) and used therein in the context of surface reconstruction to compare the performance of the DCT-based Poisson solver and the Frankot-Chellappa technique, based on the Discrete Fourier transform (DFT), with other reconstruction methods. The image represents a computer generated surface displayed as a three dimensional plot in which the vertical axis measures pixel intensity values. The range of the image is $[0..26]$ and the size of the image is 64×64 . The final step of generating the original surface is low-pass filtering for a smoothed visual aspect. As a result, in the gradient domain, all magnitudes are significantly reduced. The two components of the Hudgin aligned gradient are displayed in Fig. 5. The images shown in Fig. 6 as well as the other five used to produce the results for the comparison section are standard test images with intensity values in the range $[0..255]$.

The quality of the reconstruction was evaluated using the *relative error* of the reconstruction, given by:

$$re = \frac{\|\Phi - \Phi_{est}\|_F}{\|\Phi\|_F} \quad (32)$$

where Φ represents the original image (ground truth), Φ_{est} represents the reconstructed image, and $\|\cdot\|_F$ denotes the Frobenius norm (i.e., the square root of the sum of the squares of all elements in a matrix).

The performance of the proposed algorithm with and without the Poisson solver (i.e., Option 1 or Option 2 presented in Sect. 3.2) was compared with the DCT based Poisson solver proposed by Simchony et al. (1990), with the DFT based Frankot-Chellappa algorithm (Frankot and Chellappa 1988), with the shapelets algorithm introduced by Kovess¹ and with the global least squares (GLS) technique² described in Harker and O’Leary (2008, 2013a).

An identical setting was ensured in all experiments. For the Frankot-Chellappa and Simchony et al. and the proposed algorithm, the input considered discretization model was the Hudgin model. The gradient was converted to slant and tilt values when the shapelets algorithm was used. Finally, when the GLS algorithm (Harker and O’Leary 2008) was used, the discretization model was done as suggested by the authors (namely, centered two point difference for inner points and three points approximations for boundary points). The mean value of the image to be reconstructed was considered known and used to correct all reconstructions. For all analyzed algorithms, the mean value of the image was adjusted at the end.

¹ Source of MATLAB code: <http://www.umiacs.umd.edu/~aagrawal/software.html>; shapelets: <http://www.csse.uwa.edu.au/~pk/research/matlabfns/>.

² Source of MATLAB code: <http://www.mathworks.com/matlabcentral/fileexchange/authors/321598>.

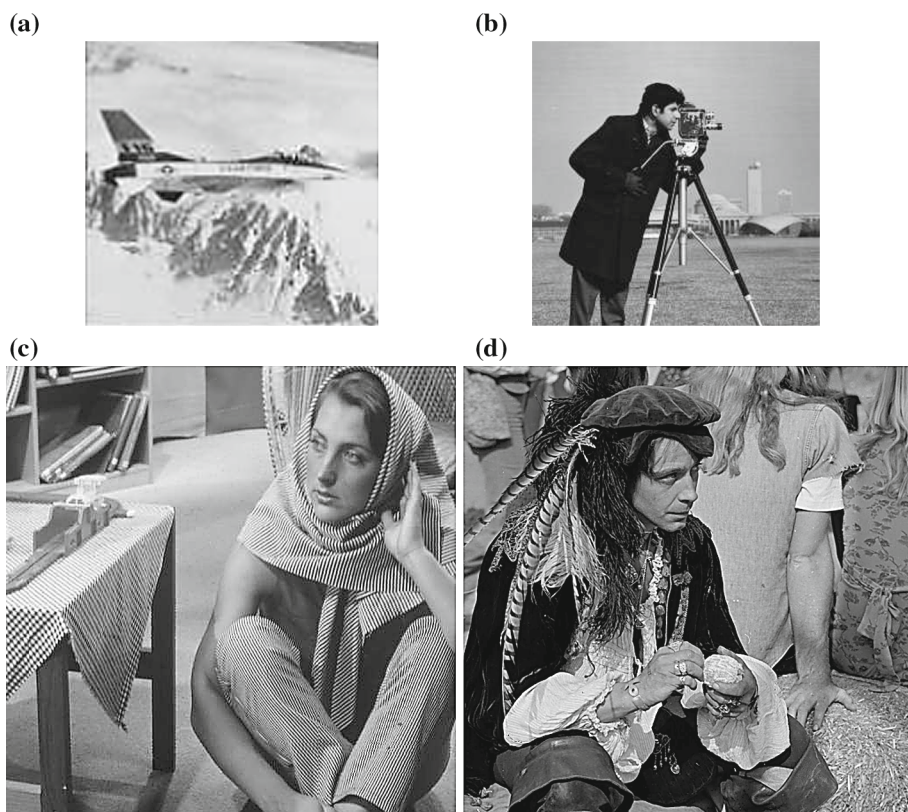


Fig. 6 Four of the test images used in the comparison. **a** Image jet 128×128 , **b** image cameraman 256×256 , **c** image barbara 512×512 , **d** image man $1,024 \times 1,024$

The relative errors of the reconstructions produced by each algorithm are displayed in Table 1. For the analyzed images, the reconstruction method proposed in this paper yielded the most accurate results, regardless of the option employed (i.e., with or without the Poisson smoothing during the synthesis step). This is expected when the input gradient is not corrupted. The method was followed closely by the DCT based Poisson solver (Simchony et al. 1990), and by the GLS technique (Harker and O’Leary 2008). The shapelets based algorithm and the DFT based Frankot and Chellappa algorithm followed, with the remark that the shapelets method produced better results for the smooth computer generated surface ramp peaks than the DFT algorithm, and ranked sixth for real images.

4.2 Gaussian white noise and impulsive noise

First, the performance of the proposed algorithm to reconstruct an image from gradient data corrupted by zero mean Gaussian white noise was evaluated in the following framework. The given gradient of the original images (same set as in Sect. 4.1) was increasingly corrupted by zero mean Gaussian white noise to cover a range of signal to noise ratios from 12dB to -6.5dB. The performance of the algorithms was thus evaluated to reconstruct a wide range of surfaces under various levels of noise corruption in the given gradient.

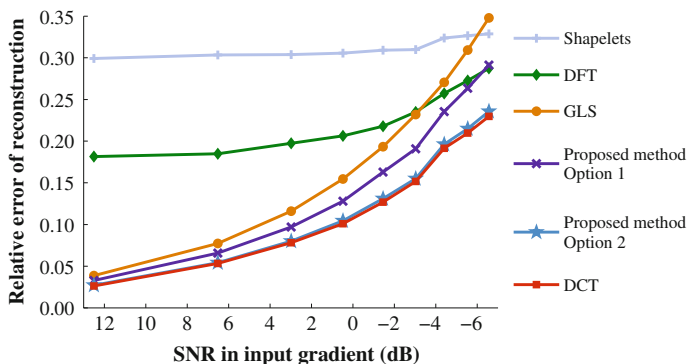


Fig. 7 Relative reconstruction error in the presence of Gaussian white noise in the input gradient

The performance of the reconstruction algorithms was evaluated by analyzing the relative error of the reconstruction as a function of SNR in the input gradient. The values illustrated in Fig. 7 represent an average of experiments performed using all the images reported in Table 1. The SNR of the gradients was the same for all algorithms. The proposed technique with the Poisson solver [using three iterations of Eq. (31)] and the DCT technique gave the best results. The proposed technique without the Poisson solver and the GLS algorithm rank third and fourth followed by the DFT and shapelets based methods. The results obtained when the proposed algorithm was used clearly show that using the Poisson solver at each resolution during the synthesis step does improve the quality of the reconstruction produced by the proposed algorithm when the input gradient is corrupted by noise.

Next, the performance of the proposed algorithm was evaluated to reconstruct an image from gradient data corrupted by outliers.

The framework in which the analysis was performed was the following. A percentage of up to 20 % of the gradient values was corrupted by impulsive noise (positive and negative outliers) and the relative error of the reconstructions obtained was computed. The magnitude of the outliers was chosen equal to the largest gradient in magnitude for the test image ramp

Table 1 Relative reconstruction error in the case of no noise in the input gradient

Image	Method 1	Method 2	Method 3	Method 4	Method 5	Method 6
ramp peaks	2.98×10^{-15}	1.46×10^{-1}	8.33×10^{-16}	1.12×10^{-16}	5.96×10^{-2}	1.74×10^{-14}
airplane	5.75×10^{-15}	1.02×10^{-1}	0	0	3.78×10^{-1}	8.35×10^{-14}
camera	1.09×10^{-13}	1.84×10^{-1}	0	0	2.34×10^{-1}	5.44×10^{-13}
clock	8.11×10^{-14}	1.20×10^{-1}	0	0	3.34×10^{-1}	3.61×10^{-13}
fruits	1.73×10^{-13}	2.90×10^{-1}	0	0	3.19×10^{-1}	1.22×10^{-12}
barbara	2.16×10^{-13}	1.49×10^{-1}	0	0	4.19×10^{-1}	2.20×10^{-12}
goldhill	3.56×10^{-13}	2.96×10^{-1}	0	0	3.75×10^{-1}	1.77×10^{-12}
peppers	2.31×10^{-13}	1.29×10^{-1}	0	0	2.55×10^{-1}	4.33×10^{-12}
lena	5.80×10^{-13}	1.79×10^{-1}	0	0	2.68×10^{-1}	9.83×10^{-12}
man	7.39×10^{-13}	2.01×10^{-1}	0	0	3.51×10^{-1}	1.71×10^{-11}

Method 1: DCT (Simchony et al. 1990); Method 2: DFT (Frankot and Chellappa 1988); Method 3: Proposed algorithm—Option 1; Method 4: Proposed algorithm - Option 2; Method 5: Shapelets (Kovesi 2005); Method 6: GLS (Harker and O’Leary 2008)

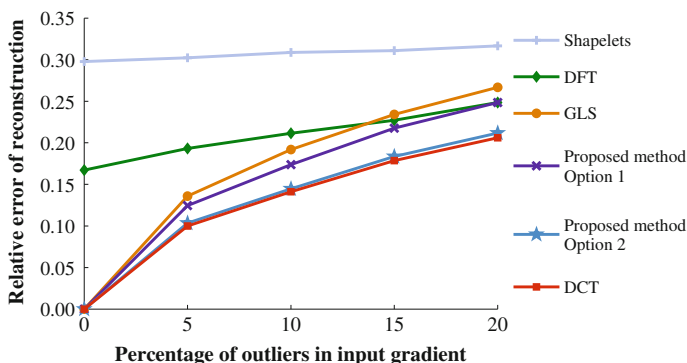


Fig. 8 Relative reconstruction error in the presence of impulsive noise (outliers) in the input gradient

peaks and of 30% of the largest gradient in magnitude for the other images. The values illustrated in Fig. 8 represent an average of all values of relative reconstruction errors obtained from similar outlier corruption levels in the given gradient. The performance of the proposed algorithm [using three iterations of Eq. (31) during synthesis] is comparable to the DCT based method. The proposed method without the Poisson solver and the GLS algorithm have a similar performance. Again, results indicate that the use of the Poisson solver (i.e., Option 2) is improving the performance of our proposed method.

4.3 Comparison with respect to computational complexity

Any comparison of algorithms in terms of computation time is determined by the implementation employed. The results presented in this section were obtained using MATLAB. However, even when the same programming platform is used, the computation time comparison is biased by built-in libraries compiled to machine code executable. So, such a comparison may not be relevant. Instead, a comparison of the algorithms in terms of the main concept which their software implementation relies on will be provided in what follows.

The main tool in the implementation of the Frankot and Chellappa technique is the DFT, while the main tool in the Simchony et al. algorithm is the DCT. The MATLAB implementation of the DCT relies on a fast Fourier transform built-in function. So, from this point of view, it can be argued that the two algorithms have similar computational complexity, with a linearithmic behaviour $\mathcal{O}(N \log N)$, where N is the number of samples of the considered signal. On the other hand, the algorithm proposed in this paper is wavelet based. The computational complexity of wavelet based algorithms is linear with respect to the number of samples in the signal, i.e., $\mathcal{O}(N)$, as shown by Hampton et al. (2008).

The experiments presented in this section indicate that the results obtained using the DCT technique and the ones obtained using the proposed algorithm are very close, with respect to the accuracy of the reconstruction. With respect to computational complexity, the proposed algorithm is $\mathcal{O}(N)$ versus $\mathcal{O}(N \log N)$, for Fourier and DCT based algorithms. The GLS algorithm, which, according to the authors discussion in Harker and O'Leary (2013b), is $\mathcal{O}(N^3)$, involves operations with sparse matrices.

5 Applications of image reconstruction from gradient

In this section, the proposed algorithm will be used in two image processing applications. The first example is stitching two images taken under different illumination conditions,

and the second example is related to image morphing. These examples illustrate how the proposed algorithm can be used in image processing applications. The Poisson solver is used at each resolution level during the reconstruction in both examples. The motivation for this choice comes from earlier studies (Perez et al. 2003; Sevcenco et al. 2011) according to which including the Poisson solver yields results with reduced visual artifacts despite the non-conservative nature of the given gradient field.

5.1 Image stitching

In image stitching (also known as image mosaicking), multiple parts of a scene are combined to produce single large representations of the scene, known as panoramas (Levin et al. 2004) or mosaics (Boutellier et al. 2008; Burt and Adelson 1983; Hsu and Wu 1996). The digital images used in such algorithms are usually partially overlapping, taken at different moments in time, by one or more cameras situated at various locations with respect to the imaged scene. These different imaging conditions generate various artifacts in the overall panorama, such as light or color inconsistencies or geometrical deformations.

Image stitching has two main stages. First, the images to be combined are spatially aligned in a stage called image registration. Next, a larger image containing all the registered images is defined and the registered images are blended together into a seamless mosaic. In the example presented in this section, the registration is done using a wavelet based technique (Yasein and Agathoklis 2007; Gillan et al. 2009), and the blending of the overlapping regions is performed in the gradient domain, similar to the method proposed by Sevcenco et al. (2011). At the end, the image is obtained from a stitched gradient data set using Option 2 of the proposed reconstruction method, extended for color images, as described at the end of Sect. 3.2. The Poisson solver is used at each resolution level during the reconstruction and the mean value in each channel is chosen to ensure a well balanced R:G:B ratio in the panoramic image. In Fig. 9c, the result obtained by applying this technique to stitch the two images³ shown in Fig. 9a, b is displayed.

5.2 Image morphing

Another interesting image processing application is image morphing. Image morphing is used to generate special effects in movies or animation by gradually modifying an image or a part thereof into another, in a seamless manner. Morphing an image into another in a video can be achieved by a sequence of frames where the initial image gradually changes into the desired one (Seitz and Dyer 1996; Wolberg 1996). In each frame, the component images must be perfectly blended to guarantee a more realistic effect. A possible approach to create such effects is object insertion or image editing (Lalonde et al. 2007; Perez et al. 2003).

The approach presented here is similar to that of Perez et al. (2003) and operates in the gradient domain. The main difference between the approach of Perez et al. and the work in this paper is that the image is reconstructed from its gradient using the method proposed in Sect. 3. The objective in the example shown in Fig. 10 is to gradually morph the face in shown in Fig. 10a to the face in Fig. 10d.⁴ This is done sequentially, to ensure a realistic and convincing transition. Specifically, a region of interest (namely, the eyes region) is first selected in Face D. In the gradient domain, the content of this region is copied to the corresponding location in the target image Face A. In Fig. 10b, the result obtained by applying the reconstruction algorithm proposed in Sect. 3 to the composite gradient thus defined is shown. The Poisson

³ The test images used in this example were downloaded from <http://www.pbase.com/ckuhn55/wyoming/>.

⁴ The images are part of the Yale Face Database.

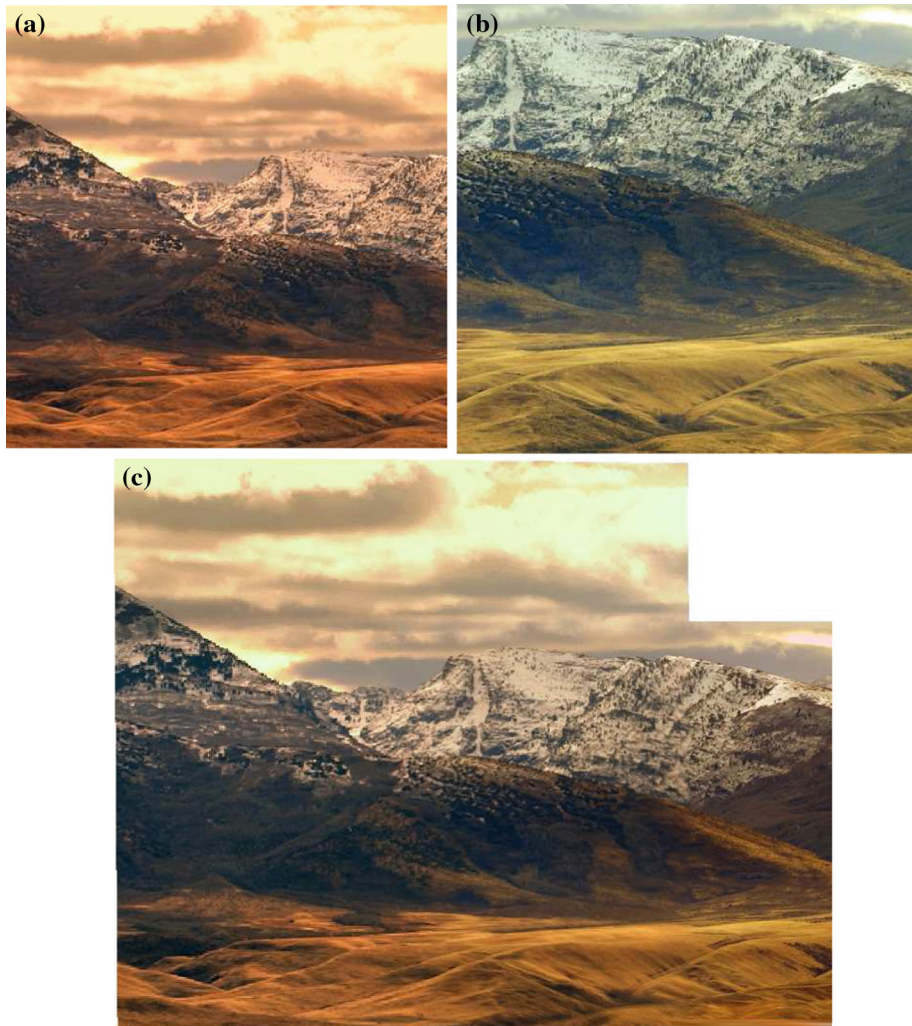


Fig. 9 Stitching two color images with differences in color and scale. **a** Input image 1, **b** input image 2, **c** result

solver is again used at each resolution level during the reconstruction. Next, this process is repeated focusing on the content of a second region of interest (namely, the mouth region) and the final result is shown in Fig. 10c. The results presented in this section clearly demonstrate that the proposed reconstruction technique can successfully be applied as a final step in the considered image processing applications.

6 Conclusions

A new image reconstruction algorithm from gradient data sets has been presented. The proposed algorithm has two main stages. First, the Haar decomposition of the image to be reconstructed is obtained from the given gradient data set. Then, the Haar wavelet synthesis is employed to produce the image. This approach represents an extension of the wavefront

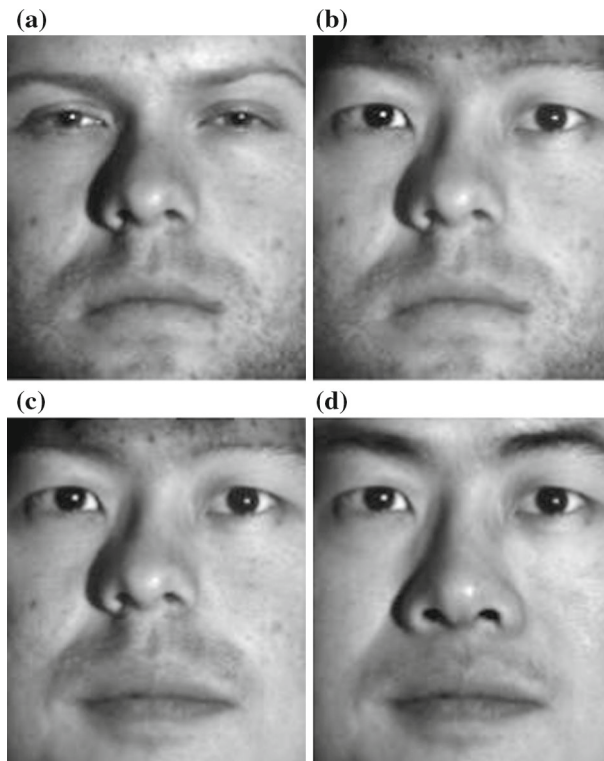


Fig. 10 Image morphing: smooth transition from Face A to Face D. **a** Face A, **b** Face B: face A with eyes of face D, **c** Face C: face B with mouth of face D, **d** Face D

reconstruction technique introduced by Hampton et al. (2008) in the context of adaptive optics. The contribution of this paper is that it extended the method of Hampton et al., such that the algorithm can be used to reconstruct images from their Hudgin aligned discrete gradient, a discretization geometry used frequently in image processing and computer vision applications. The main strengths of the algorithm lie in its $\mathcal{O}(N)$ computational complexity and in its multiresolution nature, which provides the possibility for further enhancements of the image, such as denoising or smoothing via iterative Poisson solvers at each resolution during Haar synthesis. Analysis of the performance of the proposed algorithm using test images shows that the inclusion of the Poisson solver at each resolution improves performance in the presence of noisy or outlier corrupted gradient data. Further, results indicate that the proposed technique produces comparable results in terms of solution accuracy to those obtained with well-known reference algorithms. The use of the proposed algorithm in image stitching or image morphing is illustrated, which indicates that the proposed algorithm can be used for image reconstruction as a final step in applications of image processing in the gradient domain.

Appendix 1: Algorithm proof

Given the Hudgin derivatives components Φ_x^H and Φ_y^H , the wavelet decomposition of Φ can be obtained using Eq. (19)–(26).

Proof From wavelet theory, it is known that the HH subband of the Haar wavelet decomposition of a 2D surface is given by:

$$\Phi_{HH}^{M-1} = \downarrow_2 [\Phi H_H(z_h) H_H(z_v)] \quad (33)$$

where $H_H(z)$ is the highpass analysis Haar wavelet filter described by (2) and the variables z_h and z_v indicate the horizontal and vertical direction of filtering, respectively.

With the connection between the Haar wavelet filters and discretization model in mind, we can write Eq. (33) as follows:

$$\Phi_{HH}^{M-1} = \downarrow_2 \left[\frac{\sqrt{2}}{2} \cdot \sqrt{2} \cdot \Phi H_H(z_h) H_H(z_v) \right]$$

Next, according to the observation made in Sect. 2.2, we can replace $\sqrt{2} \cdot \Phi H_H(z_h)$ with the given Φ_x^H . Doing so yields:

$$\Phi_{HH}^{M-1} = \downarrow_2 \left[\frac{\sqrt{2}}{2} \Phi_x^H H_H(z_v) \right] \quad (34)$$

$$= \downarrow_2 \left[\frac{\sqrt{2}}{4} \cdot 2 \cdot \Phi_x^H H_H(z_v) \right] \quad (35)$$

Further, we note that:

$$\begin{aligned} \Phi_x^H H_H(z_v) &= \sqrt{2} \Phi H_H(z_h) H_H(z_v) \\ &= \sqrt{2} \Phi H_H(z_v) H_H(z_h) = \Phi_y^H H_H(z_h) \end{aligned}$$

This observation allows us to replace $2\Phi_x^H H_H(z_v)$ with $\Phi_x^H H_H(z_v) + \Phi_y^H H_H(z_h)$, and so Eq. (34) becomes:

$$\Phi_{HH}^{M-1} = \downarrow_2 \left\{ \frac{\sqrt{2}}{4} [\Phi_y^H H_H(z_h) + \Phi_x^H H_H(z_v)] \right\} \quad (36)$$

This concludes the proof of Eq. (21). Please note that the downsampler in front of the square brackets of the right hand-side term is two directional (i.e., the downsampling is done horizontally and vertically). The proof of Eq. (19)–(20), and (22)–(22) can be found in Hampton et al. (2008).

Appendix 2: Performance comparison

See Tables 2 and 3

Table 2 Relative reconstruction error in the presence of white Gaussian noise

SNR in gradient	Relative error re					
	Method 1	Method 2	Method 3	Method 4	Method 5	Method 6
12.5026	0.0263	0.1815	0.0328	0.0271	0.2992	0.0387
6.5237	0.0533	0.1849	0.0657	0.0541	0.3034	0.0773
2.9838	0.0781	0.1974	0.0970	0.0800	0.3039	0.1160
0.4819	0.1010	0.2063	0.1280	0.1044	0.3056	0.1546
−1.4545	0.1269	0.2179	0.1629	0.1310	0.3092	0.1933
−3.0296	0.1517	0.2350	0.1908	0.1550	0.3099	0.2319
−4.4040	0.1915	0.2572	0.2355	0.1962	0.3237	0.2706
−5.5376	0.2097	0.2728	0.2635	0.2150	0.3265	0.3093
−6.5646	0.2297	0.2874	0.2913	0.2357	0.3288	0.3479

Method 1: DCT (Simchony et al. 1990); Method 2: DFT (Frankot and Chellappa 1988); Method 3: Proposed algorithm—Option 1; Method 4: Proposed algorithm—Option 2; Method 5: Shapelets (Kovesi 2005); Method 6: GLS (Harker and O’Leary 2008)

Table 3 Relative reconstruction error in the presence of outliers

Outlier percentage in gradient	Relative error re					
	Method 1	Method 2	Method 3	Method 4	Method 5	Method 6
0	4.95×10^{-13}	0.1505	2.23×10^{-17}	1.12×10^{-17}	0.2998	3.75×10^{-12}
5	0.1012	0.1851	0.1247	0.1041	0.3038	0.1404
10	0.1380	0.2013	0.1701	0.1416	0.3111	0.1953
15	0.1750	0.2287	0.2132	0.1797	0.3145	0.2382
20	0.2072	0.2454	0.2479	0.2124	0.3196	0.2741

Method 1: DCT (Simchony et al. 1990); Method 2: DFT (Frankot and Chellappa 1988); Method 3: Proposed algorithm—Option 1; Method 4: Proposed algorithm—Option 2; Method 5: Shapelets (Kovesi 2005); Method 6: GLS (Harker and O’Leary 2008)

References

- Agrawal, A., & Raskar, R. (2006). What is the range of surface reconstructions from a gradient field. In *Proceedings of the European conference on computer vision* (pp. 578–591).
- Agrawal, A., Raskar, R., Nayar, S. K., & Li, Y. (2005). Removing photography artifacts using gradient projection and flash-exposure sampling. *ACM Transactions on Graphics*, 24(3), 828–835.
- Boutellier, J., Silvén, O., Tico, M., Korhonen, L., et al. (2008). Objective evaluation of image mosaics. In J. Braz (Ed.), *Computer vision and computer graphics. Theory and applications* (pp. 107–117). Berlin, Heidelberg: Springer.
- Burt, P., & Adelson, E. (1983). A multiresolution spline with application to image mosaics. *ACM Transactions on Graphics*, 2, 217–236.
- Craine, B., Craine, E., O’Toole, C., & Ji, Q. (1998). Digital imaging colposcopy: Corrected area measurements using shape-from-shading. *IEEE Transactions on Medical Imaging*, 17(6), 1003–1010.
- Fattal, R., Lischinski, D., & Werman, M. (2002). Gradient domain high dynamic range compression. *ACM Transactions on Graphics*, 21(3), 249–256.
- Finlayson, G., Hordley, S., & Drew, M. (2002). Removing shadows from images. In *Proceedings of the European conference on computer vision* (pp. 823–836).
- Frankot, R., & Chellappa, R. (1988). A method for enforcing integrability in shape from shading algorithms. *IEEE Transactions on Pattern Analysis and Machine Intelligence*, 10, 439–451.

- Fried, D. (1977). Least square fitting a wavefront distortion estimate to an array of phase difference measurements. *Journal of the Optical Society of America*, 67, 370–374.
- Gillan, S., Agathoklis, P., & Yasein, M. (2009). A feature based technique for face recognition using Mexican hat wavelets. In *IEEE Pacific rim conference on communications, computers and signal processing* (pp. 792–797).
- Gilles, L., Vogel, C., & Ellerbroek, B. L. (2002). Multigrid preconditioned conjugate-gradient method for large-scale wave-front reconstruction. *Journal of the Optical Society of America*, 19(9), 1817–1822.
- Hampton, P., & Agathoklis, P. (2010). Comparison of Haar wavelet-based and Poisson-based numerical integration techniques. In *Proceedings of IEEE international symposium on circuits and systems* (pp. 1623–1626).
- Hampton, P., Agathoklis, P., & Bradley, C. (2008). A new wave-front reconstruction method for adaptive optics system using wavelets. *IEEE Journal of Selected Topics in Signal Processing*, 2(5), 781–792.
- Hampton, P., Agathoklis, P., & Bradley, C. (2009). Wavefront reconstruction over a circular aperture using gradient data extrapolated via the mirror equations. *Applied Optics*, 48(20), 4018–4030.
- Harker, M., & O’Leary, P. (2008). Least squares surface reconstruction from measured gradient fields. In *IEEE conference on computer vision and pattern recognition. CVPR* (pp. 1–7).
- Harker, M. & O’Leary, P. (2013a). Direct regularized surface reconstruction from gradients for industrial photometric stereo. *Computers in Industry* doi:10.1016/j.compind.2013.03.013.
- Harker, M. & O’Leary, P. (2013b). Regularized reconstruction of a surface from its measured gradient field. <http://arxiv.org/pdf/1308.4292.pdf>.
- Hertzmann, A., & Seitz, S. (2005). Example-based photometric stereo: shape reconstruction with general, varying BRDFs. *IEEE Transactions on Pattern Analysis and Machine Intelligence*, 27(8), 1254–1264.
- Hsu, C.-T., & Wu, J.-L. (1996). Multiresolution mosaic. *IEEE Transactions on Consumer Electronics*, 42(4), 981–990.
- Hudgin, R. (1977). Wave-front reconstruction for compensated imaging. *Journal of the Optical Society of America*, 67, 375–378.
- Kovesi, P. (2005). Shapelets correlated with surface normals produce surfaces. In *ICCV05* (pp. 994–1001).
- Lalonde, J.-F., Hoiem, D., Efros, A. A., Rother, C., Winn, J., & Criminisi, A. (2007). Photo clip art. *ACM Transactions on Graphics*, 26. <http://dl.acm.org/citation.cfm?id=1275808.1276381&coll=DL&dl=ACM&CFID=257078954&CFTOKEN=11593042>.
- Levin, A., Zomet, A., Peleg, S., & Weiss, Y. (2004). Seamless image stitching in the gradient domain. In *Proceedings of the European conference on computer vision*, (Vol. 4, pp. 377–389).
- Perez, P., Gangnet, M. & Blake, A. (2003). Poisson image editing. In *Proceedings of SIGGRAPH’03*, (pp. 313–318).
- Poyneer, L. A., & Véran, J.-P. (2005). Optimal modal Fourier-transform wavefront control. *Journal of the Optical Society of America*, 22(8), 1515–1526.
- Rash, C. E., Russo, M. B., Letowski, T. R. & Schmeisser, E. T. (eds.) (2009). *Helmet-Mounted displays: sensation, perception and cognition issues*, U.S. Army Aeromedical Research Laboratory, Fort Rucker, Alabama, USA, Chap. 10.
- Reddy, D., Agrawal, A., & Chellappa, R. (2009). Enforcing integrability by error correction using ℓ_1 -minimization (pp. 2350–2357). In *IEEE Conference on computer vision and pattern recognition*.
- Seitz, S. M., & Dyer, C. R. (1996). View morphing. In *Proceedings of SIGGRAPH’96*, (pp. 21–30).
- Sevcenco, I. S., Hampton, P. J., & Agathoklis, P. (2011). Seamless stitching of images based on a Haar wavelet 2D integration method. In *17th International conference on digital signal processing (DSP)* (pp. 1–6).
- Simchony, T., Chellappa, R., & Shao, M. (1990). Direct analytical methods for solving Poisson equations in computer vision problems. *IEEE Transactions on Pattern Analysis and Machine Intelligence*, 12, 435–446.
- Smith, W. A. P., & Hancock, E. (2006). Face recognition using 2.5D shape information. In *Proceedings of IEEE computer society conference on computer vision and pattern recognition*, (Vol. 2, pp. 1407–1414).
- Tumblin, J., Agarwal, A., & Raskar, A. (2005). Why I want a gradient camera. In *Proceedings of IEEE computer society conference on computer vision and pattern recognition* (Vol. 1, pp. 103–110).
- Vetterli, M., & Kovačević, J. (1995). *Wavelets and subband coding*. Englewood Cliffs, NJ: Prentice-Hall.
- Vogel, C. R., & Yang, Q. (2006). Multigrid algorithm for least-squares wavefront reconstruction. *Applied Optics*, 45(4), 705–715.
- Watkins, D. S. (2002). *Fundamentals of matrix computations*. New York, USA: Wiley.
- Wolberg, G. (1996). Recent advances in image morphing. In *Proceedings of the 1996 conference on computer graphics, international* (pp. 64–71).
- Yasein, M., & Agathoklis, P. (2007). A robust, feature-based algorithm for aerial image registration. In *IEEE international symposium on industrial electronics* (pp. 1731–1736).

Author Biographies



Ioana S. Sevcenco received a B.Sc. and M.Sc. degree in mathematics from University of Bucharest, Romania, in 2002, and 2004, respectively. In 2012, she received a M.A.Sc. degree in electrical and computer engineering from the University of Victoria, Victoria, BC, Canada. Currently, she is pursuing her Ph.D. degree with the same department. Her academic assistant work in the electrical and computer engineering department at the University of Victoria brought her two nominations for the university-wide excellence in graduate teaching award. In addition, she was the recipient of the departmental excellence in graduate teaching award in 2012. In 2012–2013, she was a teaching assistant consultant, mentoring over 100 academic assistants in the faculty of engineering. Her commitment to academic excellence earned her two fellowships and a graduate studies award in 2010, 2012 and 2013 from the University of Victoria. She has been an IEEE graduate student member since 2011. Her teaching and research interests are in the areas of digital signal processing, with applications in image and video processing.



Peter J. Hampton received his Ph.D. at the University of Victoria for his work in developing the wavelet based method for reconstructing 2.5D shapes from gradient data. The process was applied to the field of Adaptive Optics, a field that greatly improves the seeing from land based telescopes. Specifically it was applied to a Woofer-Tweeter arrangement of co-operative deformable mirrors. This work was nominated by the University of Victoria as their top eligible Ph.D. for the NSERC Silver Medal (awarded to the top two engineering and sciences Ph.D. for 2009 in Canada). It achieved a top 10 national standing. Peter currently works for Cellula Robotics Ltd. as a Control Systems Engineer, EIT, where he develops the control and automation for robotics that are used to explore deep under the ocean.



Panajotis Agathoklis received the Dipl.-Ing. degree in electrical engineering and the Dr.Sc.Tech. degree from the Swiss Federal Institute of Technology, Zurich, Switzerland, in 1975 and 1980, respectively. From 1981 until 1983, he was with the University of Calgary as a Post-Doctoral Fellow and part-time Instructor. Since 1983, he has been with the Department of Electrical and Computer Engineering, University of Victoria, BC, Canada, where he is currently a Professor. He has received a NSERC University Research Fellowship and Visiting Fellowships from the Swiss Federal Institute of Technology, from the Australian National University and the University of Perth, Australia. He is a Fellow of the Engineering Institute of Canada. He has been member of the Technical Program Committee of many international conferences and has served as the Technical Program Chair of the 1991 IEEE PACRIM Conference, the 1998 IEEE Symposium on Advances in Digital Filtering and Signal Processing and the 2009 ISSPIT. His fields of interest are in control, digital signal processing and their applications. He worked in the stability of multidimensional systems, applications of

2D and 3D filtering, image reconstruction from gradient data and its applications in adaptive optics.